




# Comparison of chemical bath-deposited ZnO films doped with Al, Ga and In

S. Edinger<sup>1,3,\*</sup> , N. Bansal<sup>1</sup>, M. Bauch<sup>1</sup>, R. A. Wibowo<sup>1</sup>, R. Hamid<sup>2</sup>, G. Trimmel<sup>3</sup>, and T. Dimopoulos<sup>1,\*</sup>

<sup>1</sup>Photovoltaic Systems, Center for Energy, AIT - Austrian Institute of Technology, Giefinggasse 2, 1210 Vienna, Austria

<sup>2</sup>Electric Drive Technologies, Center for Low-Emission Transport, AIT - Austrian Institute of Technology, Giefinggasse 2, 1210 Vienna, Austria

<sup>3</sup>Institute for Chemistry and Technology of Materials, NAWI Graz, Graz University of Technology, Stremayrgasse 9, 8010 Graz, Austria

Received: 13 November 2016

Accepted: 17 April 2017

Published online:

28 April 2017

© The Author(s) 2017. This article is an open access publication

## ABSTRACT

A comparative study is presented on chemical bath-deposited ZnO films, doped with the group-13 metals Al, Ga and In. The study reveals marked differences in dopant incorporation in the films, which increases in the order: In, Al and Ga. The presence of dopant in the solution induces significant modifications in the deposition rate, which varies between 110 and 40 nm min<sup>-1</sup>. All films are (002)-textured, whereas the lattice stress evolution with the dopant type and concentration suggests that Ga has the highest degree of substitutional incorporation in Zn sites. The average visible transmittance is higher than 80%, while the infrared reflectivity depends on the free carrier density in the films, which is the lowest for undoped ZnO and increases in the order: In-, Al- and Ga-doped ZnO. Optical measurements also yield an inverse correlation between carrier density and mobility. Doping enlarges the bandgap, as well as the Urbach energy that is related to the films' disorder. The lowest electrical resistivity, measured by four-point probe, is  $1.7 \times 10^{-2} \Omega \text{ cm}$  and is obtained for In-doped films after being exposed to ultraviolet light. Ga-doped films are found to exhibit the highest stability of the conductivity upon ultraviolet exposure.

## Introduction

Zinc oxide (ZnO) is a wide bandgap semiconductor with unique chemical, optical and electrical properties that render it an indispensable material component in modern optoelectronic devices, solar cells, piezoelectric transducers, chemical and gas sensors, catalysis and other applications [1–5]. One characteristic in the

chemistry of zinc is the tendency of zinc hydroxide to easily undergo dehydration reactions forming the oxide phase, which allows to obtain high ZnO crystal quality even for low-temperature processing [6]. This makes the material interesting for solution processing, such as chemical bath deposition (CBD), which produces thin films in a controlled precipitation step from supersaturated solutions [7].

Address correspondence to E-mail: Stefan.Edinger.fl@ait.ac.at; Theodoros.Dimopoulos@ait.ac.at

Richardson and Lange introduced a method for the CBD growth of ZnO, which relies on the temperature-dependent retrograde solubility of mixed zinc ammonia hydroxide complexes in a basic, aqueous environment [8]. This concept was used by several groups to deposit intrinsic [9] and doped ZnO thin films [10–14]. The key to obtain dense materials rather than nanorods was in all approaches the use of citrate as structure-directing agent, which selectively decelerates crystal growth along the ZnO c-axis [9, 15]. Hagendorfer et al. reported Al-doped ZnO layers with resistivity values in the range of  $10^{-3} \Omega \text{ cm}$ , using the aforementioned CBD chemistry. To achieve low resistivity values, ultraviolet (UV)-light annealing instead of thermal annealing was used, permitting to maintain the temperature below 85 °C during the whole production process [10, 11].

The studies in the literature have dealt either with Al-doped [10, 11, 13] or with Ga-doped [12, 14] ZnO. Due to differences in the used recipes and reactor designs, it is hard to make a conclusive comparison on the effect of the different dopants on the processing and properties of the doped films. Even in reports concerning the same dopant, significant differences are observed. For instance, Hagendorfer et al. report a drastic change in the ZnO grain morphology for  $\text{Al}(\text{NO}_3)_3$  concentrations higher than 5 mM [10], while Miyake et al. do not observe such an effect despite using dopant concentrations up to 10 mM [13].

In this study, the ammonia-based CBD method was employed to deposit undoped and doped ZnO films. The effects of doping with the group-13 metals Al, Ga and In on the processing, the morphology, the optical and the electrical properties of the films were systematically compared and analyzed. Distinctively and complementary to the existing literature on the topic, this work allows a direct comparison between the different doped materials, as they were prepared using the same basic recipe and reactor, varying only the type and concentration of the dopant. The impact on the optical and electrical properties is investigated with respect to the actual dopant concentration in the films. Furthermore, the effects of the dopants on the UV stability of the materials are discussed.

## Experimental

### Film deposition

Microscope glass slides (VWR,  $2.5 \times 2.5 \text{ cm}^2$ ) were used as substrates. They were cleaned with

Hellmanex III detergent and rinsed with ultrapure water and isopropanol prior to the depositions. A ZnO seed layer was deposited on the glass substrates prior to the CBD, following a route developed by Fuchs et al. [11]. An appropriate amount of ZnO (Sigma-Aldrich 205532) was dissolved in 5 M  $\text{NH}_4\text{OH}$  (Sigma-Aldrich 221228) in order to obtain a 50-mM ZnO solution. This was then spin-coated (2500 rpm, 1 min) on the glass substrate, which was heated afterward to 100 °C for 5 min.

For the CBD itself, 123 mM ZnO (Sigma-Aldrich 205532), 1 mM citric acid (Sigma-Aldrich 251275) and 62.5 mM ammonium nitrate (VWR 100303S) were transferred into a 1-M aqueous ammonia solution, obtained by mixing ultrapure water (18.2 M $\Omega$ ) with concentrated ammonium hydroxide solution (Sigma-Aldrich 221228). The resulting solution had a pH value of 11.4. This suspension was stirred overnight, and the residual solid was separated on the next day using a filter membrane (Whatman 7060-4710, 1  $\mu\text{m}$  pore diameter). The zinc concentration in the obtained clear solution was 50 mM, as determined by inductively coupled plasma-optical emission spectroscopy (ICP-OES). 200 ml of this solution were transferred into a 200-ml beaker, heated to 85 °C within 20 min and stirred with a magnetic stirrer at 420 rpm. Doping was achieved by adding appropriate amounts of 0.5 M aqueous solutions of  $\text{Al}(\text{NO}_3)_3$  (Sigma-Aldrich 229415),  $\text{Ga}(\text{NO}_3)_3$  (Sigma-Aldrich 289892) and  $\text{In}(\text{NO}_3)_3$  (Sigma-Aldrich 326135), in order to obtain Al-doped (AZO), Ga-doped (GZO) and In-doped ZnO (IZO) films, respectively. Four concentrations (1, 2, 3 and 4 mM) were used for each dopant element. In the following, samples with increasing Al concentration are designated as: AZO-1 to AZO-4 and similarly for the other dopant elements. When the solution reached 80 °C, the seeded substrate was placed into a custom-build Teflon holder, which was immersed typically for 30 min. In certain cases where the doping caused lower deposition rates, the deposition time was raised correspondingly to obtain films of comparable thickness. Directly after deposition, the samples were annealed under UV illumination ( $43.2 \text{ J cm}^{-2}$ , UVA).

### Characterization techniques

The exact dopant concentration in the solution was experimentally determined by ICP-OES (PerkinElmer Optima 2100 DV). This technique was further used to

determine the dopant metal-to-Zn ratio in the materials by etching the films with nitric acid and analyzing the resulting solution.

The thickness, the grain size and the morphology of the samples were investigated by cross-sectional and plane-view scanning electron microscopy (SEM, Supra 40, Carl Zeiss), using an in-lens detector and 5 kV acceleration voltage. Crystallographic information was acquired by X-ray diffraction (XRD, XPERT PRO powder). Optical transmission data were recorded with a Fourier-transform spectrometer (FTIR, Bruker Vertex 70) in the range of 0.3–2.5  $\mu\text{m}$ . The same instrument was used to record reflectivity spectra at an angle of  $13^\circ$ . The sheet resistance of the materials was measured by standard four-point probe technique.

## Results and discussion

### Dopant incorporation

The dopant concentration in the films was quantified by OES, yielding the results shown in Fig. 1 and in Table 1. A linear increase of the dopant concentration in the films can be observed with increasing dopant concentration in the solution for both AZO and GZO. The degree of Ga incorporation is, however, more pronounced. Indium, on the other hand, shows only a slight incorporation of 0.06 at.%, which remained unaffected by a further increase of dopant in the solution.

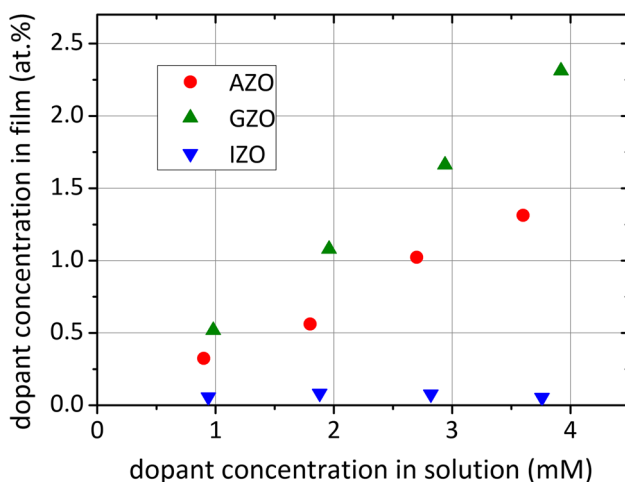


**Figure 1** Dopant concentration in the film versus dopant concentration in the solution.

This observation can be explained by the differences in the solubility of the group-13 elements, calculated using the PHREEQC software kit [16] with thermodynamic data of the Thermoddem database, provided by the BRGM institute [17]. The following two assumptions were made: (a) the interaction of the group-13 species with ammonia was neglected, as their  $K_1$  values in regard to hydroxide are at least six orders of magnitude higher than for the ammonia ligand [18]. (b) The interaction of the metal ions with the citrate anion is neglected, as pronounced adsorption is expected for this species due to its affinity to the (002) facet of ZnO. Consequently, the dopant solubility is calculated by its interaction with the hydroxide anion, resulting in the values plotted in Fig. 2 for a temperature of  $85^\circ\text{C}$ , as a function of the solution pH.

Ga has the highest solubility under basic conditions, which is an order of magnitude higher than that of Al. Indium is barely soluble under the pH regime of this study, in agreement with its minimal incorporation seen in the films (Fig. 1). This became also apparent during the CBD experiments, as the addition of In resulted in a turbid solution for all concentrations. On the contrary, Al and Ga both gave initially clear solutions, which became turbid during deposition due to homogeneous nucleation taking place. The latter depends on the solution supersaturation and is therefore directly related to the solubility of the species. It was also systematically observed that the precipitation was more pronounced in solutions containing  $\text{Al}^{3+}$  than for formulations with  $\text{Ga}^{3+}$ .

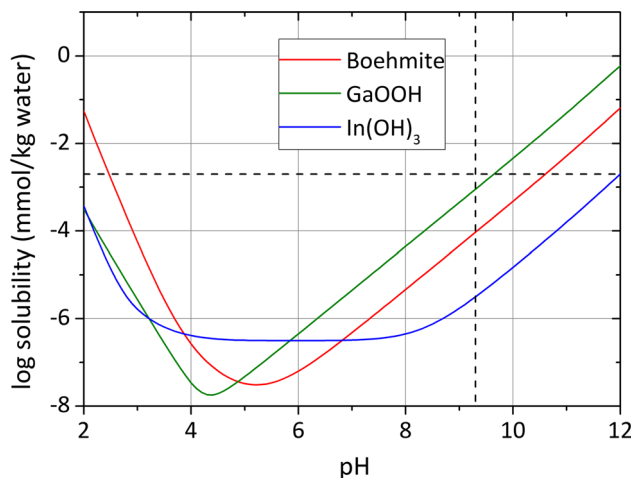
### Morphology and structural properties

Figure 3 shows selected cross-sectional and plane-view SEM images from undoped and doped ZnO films. Further micrographs are available in the supplementary information (Fig. S1). The films exhibit a spatially confined, oriented growth mode, typical for ZnO grown by this technique [9]. In the early stages of the CBD, the polycrystalline seed layer promotes the growth of randomly oriented crystals. The ones oriented along the fastest growth direction, which is the polar (001) orientation (*c*-axis), will overtake their less favorably oriented neighboring crystals, bringing their growth to an end. As the result of this competitive growth, the film is composed of quasi-parallel columns along the *c*-axis, which can be observed

**Table 1** Summary of the films' properties, including the dopant incorporation in the material, the sample thickness, the average grain size, the position of the (002) reflection, the optical

bandgap  $E_G$ , the Urbach energy  $E_U$ , the optical carrier concentration  $N_{opt}$  and mobility  $\mu_{opt}$ , the optical resistivity  $\rho_{opt}$  and the electrical resistivity  $\rho_{4p}$

#	Dop. inc. (at.%)	Thickness ( $\mu\text{m}$ )	Grain size (nm)	(002) peak pos. ( $^\circ$ )	$E_G$ (eV)	$E_U$ (meV)	$N_{opt}$ ( $\text{cm}^{-3}$ )	$\mu_{opt}$ [ $\text{cm}^2/(\text{Vs})$ ]	$\rho_{opt}$ ( $\Omega \text{ cm}$ )	$\rho_{4p}$ ( $\Omega \text{ cm}$ )
ZnO	0	2.68	230	34.357	3.37	46.37	$3.31 \times 10^{19}$	29.12	0.0064	0.0589
AZO-1	0.32	2.89	261	34.364	3.48	48.38	$1.25 \times 10^{20}$	17.21	0.0029	0.0237
AZO-2	0.56	2.63	263	34.374	3.50	48.58	$1.11 \times 10^{20}$	17.40	0.0032	0.0166
AZO-3	1.02	2.60	257	34.377	3.50	52.49	$1.34 \times 10^{20}$	14.17	0.0032	0.0208
AZO-4	1.31	2.20	195	34.432	3.48	73.90	$1.66 \times 10^{20}$	12.69	0.003	0.0154
GZO-1	0.52	3.06	252	34.379	3.45	53.04	$1.81 \times 10^{20}$	10.3	0.0033	0.0229
GZO-2	1.08	2.89	282	34.387	3.46	58.94	$2.68 \times 10^{20}$	8.31	0.0028	0.0222
GZO-3	1.66	2.24	283	34.389	3.46	66.51	$3.32 \times 10^{20}$	7.78	0.0024	0.0265
GZO-4	2.31	2.27	295	34.404	3.48	62.40	$3.31 \times 10^{20}$	6.53	0.0029	0.0191
IZO-1	0.06	2.93	246	34.367	3.41	48.27	$3.35 \times 10^{19}$	23.68	0.0079	0.0214
IZO-2	0.08	3.04	303	34.368	3.40	45.60	$5.60 \times 10^{19}$	22.87	0.0049	0.0167
IZO-3	0.08	2.84	294	34.366	3.39	48.49	$5.12 \times 10^{19}$	23.90	0.0051	0.0199
IZO-4	0.05	3.40	321	34.351	3.41	47.52	$4.30 \times 10^{19}$	28.03	0.0052	0.0167



**Figure 2** Solubility diagram of the most stable metal hydroxide phases at 85 °C versus the solution pH.

in the electron micrographs. While the plane view of the undoped film reveals sparsely dispersed voids (inset of Fig. 3a), a densification is observed upon introduction of dopants into the solution (Fig. 3b–d).

The dopant addition into the solution affects the growth rate of the films (Fig. 4a). This depends on the concentration and type of the dopant. For Al, the growth rate decreases with dopant concentration, from the initial 90  $\text{nm min}^{-1}$  for the undoped film to 40  $\text{nm min}^{-1}$  for the AZO-4 sample. The IZO films, on the other hand, show a tendency for increased growth rate with dopant concentration. While the GZO-1 and GZO-2 films were deposited at a higher

growth rate compared to undoped ZnO, the growth rate was considerably smaller for GZO-3 and GZO-4. The synergetic effects of the following mechanisms may explain this behavior.

Firstly, the addition of metal nitrates into the bath results in a slight decline in the pH value from initially 11.38 (ZnO) down to 11.15 (AZO-4). In their thermodynamic modeling, Richardson and Lange showed that the minimum in ZnO solubility lies between pH 10 and 11 [8]. Thus, the pH decrease is expected to lead to an increase of the supersaturation during deposition, which in turn leads to higher growth rates. To verify this hypothesis, additional undoped samples were grown from solutions, whose pH values were matched to the dopant-containing baths by adding ammonium nitrate prior to the deposition. Indeed, in these experiments an increase in the growth rate could be observed.

The second mechanism, which is often reported for the CBD of AZO films, is the ability of  $\text{Al}(\text{OH})_4^-$  to impede the growth along the c-axis [10, 19, 20]. This is manifested in the experiments by a marked reduction of the growth rate for the AZO films. Ga exhibits similar chemistry with the formation of  $\text{Ga}(\text{OH})_4^-$  [22], and a similar decline in growth rate can be observed, albeit less pronounced than the Al case. The synergetic effect of the two aforementioned mechanisms can explain the initial increase and then the subsequent decline of the growth rate at high Ga concentrations.

Due to the significant reduction in the deposition rate, a second sample series of AZO was synthesized,

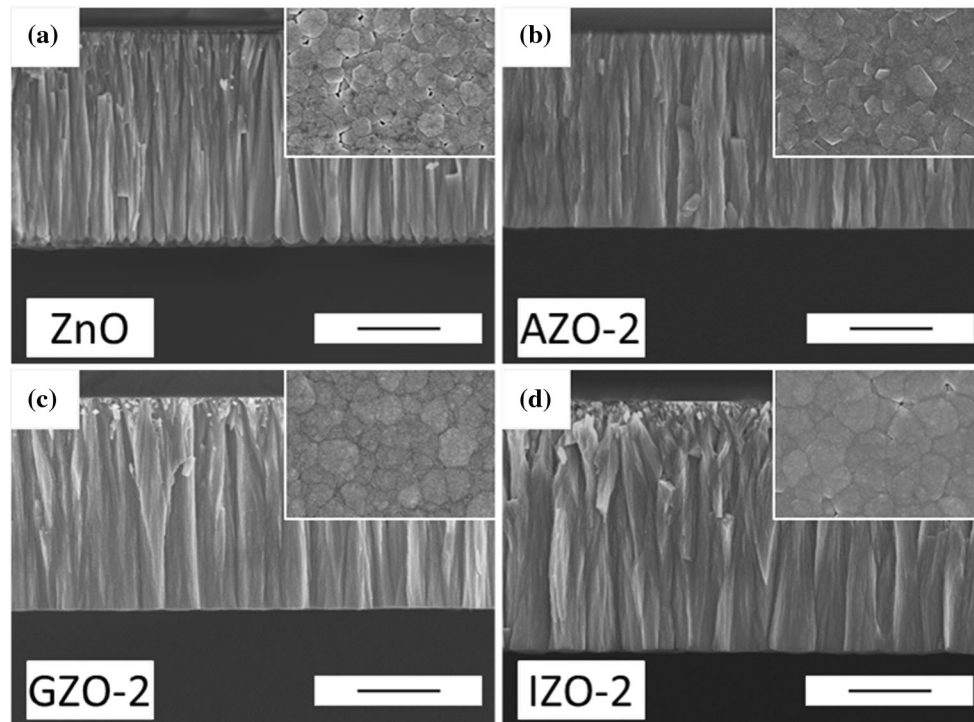
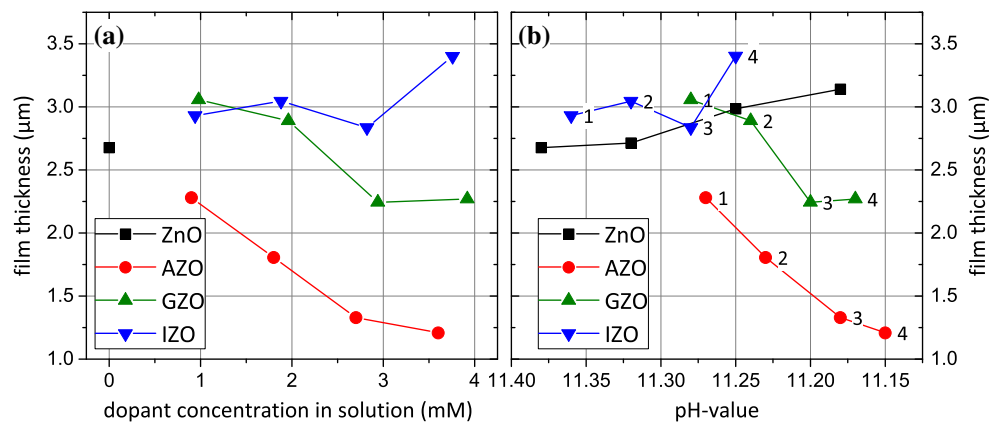


**Figure 3** Cross-sectional SEM images from films of **a** undoped ZnO, **b** AZO-2, **c** GZO-2 and **d** IZO-2. The *insets* show the plane-view images of the corresponding films. The *scale bar* corresponds to 1  $\mu\text{m}$ .

**Figure 4** **a** Film thickness after a deposition time of 30 min versus the dopant concentration in the solution, **b** film thickness versus the pH value in the solution.

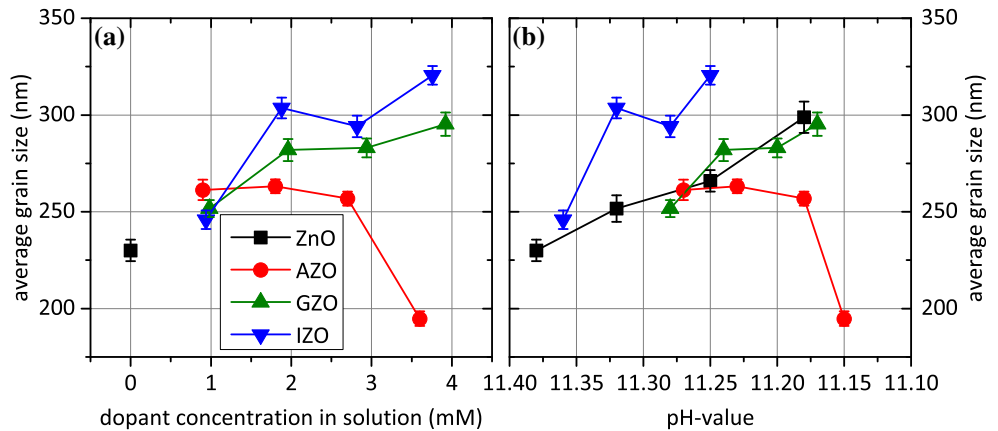


for which the deposition time was extended where necessary, in order to obtain comparable film thicknesses in the range of 2.7  $\mu\text{m}$ . The reason for this was to be able to compare the electrical properties of the different doped films, as the resistivity of materials grown by this technique is known to have a thickness dependence [21]. However, for the highest Al doping, it was not possible to grow a film thicker than 2.2  $\mu\text{m}$  even after prolonging the deposition time from the typical 30 to 90 min (using a single bath). This shows that, under these conditions, the film growth is

decelerated by the pronounced precipitation in the solution.

Plane-view micrographs were used to estimate the grain size of the materials, which was derived by counting the number of grain boundaries intersecting lines drawn on the images. For each film, we used 15 SEM images, which were obtained from different locations on the sample. Figure 5 and Table 1 report the average value of the grain size. Introducing Ga into the solution leads to a steady increase in grain size from  $\sim 225$  nm for the undoped films up to an

**Figure 5** Average grain size diameters as obtained from plane-view electron micrographs, shown versus **a** the dopant concentration in solution and **b** the pH value.



average of  $\sim 300$  nm. This can be explained by the lower pH value in the deposition solution caused by the dopant addition, as the grain size of the reference ZnO materials showed a similar behavior in dependence of the pH value (see Fig. 5b). Although In exhibited limited incorporation in the films and solubility (see “Dopant incorporation” section), its addition into the solution still had an effect on the grain size, with a maximum of 321 nm obtained for the IZO-4 sample. This increase might stem from structure-directing properties of the dopant but also from the increased film thickness of this sample series. Al on the other hand showed after an initial increase at low concentrations a significant decrease for the AZO-4 film, which is associated with the change in crystal shape (see Fig. S1).

Almost all diffractograms for the undoped and doped ZnO films, shown in Fig. 6a, exhibit predominantly the (002) reflection of zincite (ICDD 00-036-1451) at  $34.4^\circ$  and its weak second-order analogue at  $75.4^\circ$ . In some materials, also the (100) plane at  $30.95^\circ$ , the (101) plane at  $36.27^\circ$  and the (103) plane at  $62.83^\circ$  can be observed, but their size is minimal. The origin of these reflections lies most probably in the lowest, randomly oriented part of the films, as described above. The only exception is the diffractogram of the highest doped AZO-4 sample, where the (103) reflection is the second highest in a number of other peaks, which can be assigned to the (102) plane at  $47.53^\circ$ , the (112) plane at  $67.93^\circ$  and (104) plane at  $81.31^\circ$ , indicating that the c-axis texture is distorted at this Al concentration. No extra impurity phases could be observed for any of the investigated films.

While the basic diffraction pattern remained the same, a small shift could be observed for the (002) peak position, which is attributed to the

incorporation of metal dopants in the lattice. Al and Ga are, with a size of 39 and 47 pm, respectively, smaller than Zn (60 pm in tetrahedral coordination) [23]. Their substitutional incorporation on Zn sites should lead to a ZnO host lattice shrinkage, shifting the Bragg reflection to higher angles. Due to the size difference, the effect should be more pronounced for Al than for Ga. However, as can be seen in Fig. 7, the opposite is the case and the GZO samples exhibit the highest shift except for the AZO-4 film, in which the (002) texture was lost. The behavior of the other AZO films can be explained considering that Al is much more prone to occupy interstitial sites [24], which tend to expand the crystal lattice by pushing their nearest neighbors. Another explanation can be that Al is partly incorporated through the formation of secondary phases [25, 26]. However, if such phases are present in the materials, they are below the detection limit of the XRD measurements. The IZO materials, on the other side, exhibit only a small shift to higher angles, which can be attributed to the low In incorporation in the films, its similar size to Zn and its tendency for substitutional incorporation [27].

### Optical and electrical properties

Figure 8a–d shows the transmittance spectra of the undoped and doped films, grouped as a function of their doping concentration. All films exhibited average specular transmittance values higher than 80% (including the substrate) in the range from 400 to 1000 nm. Distinct Fabry–Perot fringes are notable, which emphasize the low surface roughness of the films. A reduction of the transmittance is observed in the longer wavelength regime due to free carrier absorption. This effect intensifies in the order:

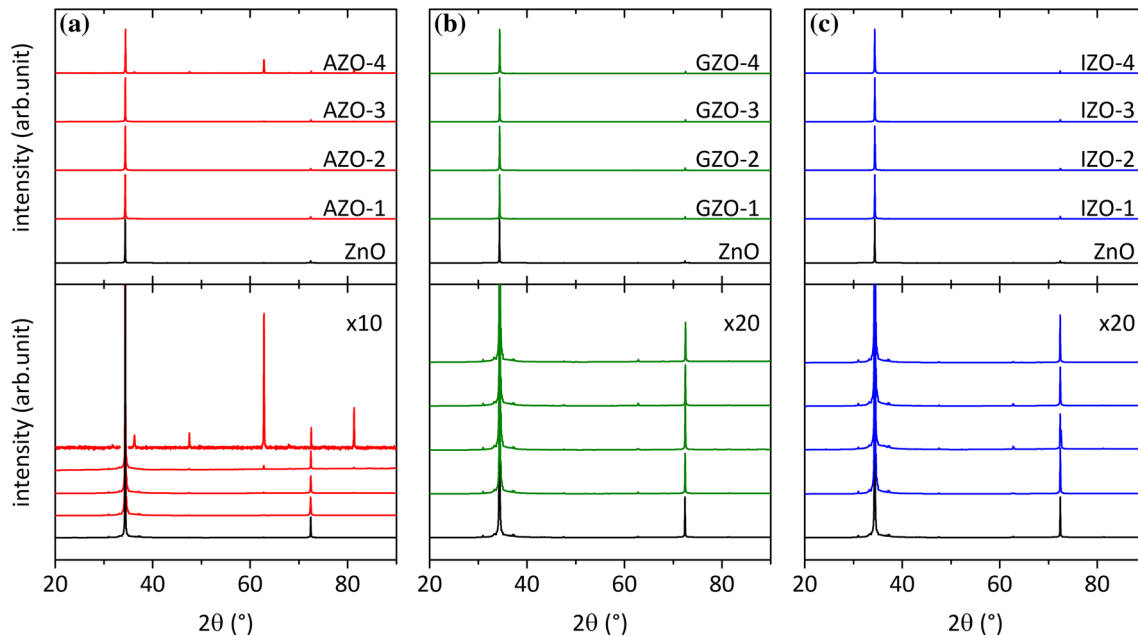


**Figure 6** X-ray diffractograms from the undoped and doped ZnO films of similar thickness. **a** AZO—series **b** GZO—series **c** IZO—series. Magnifications of the diffractograms are shown.

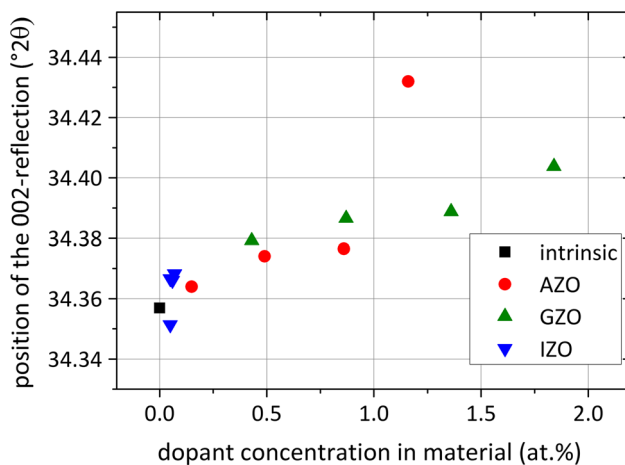


**Figure 7** Position of the (002) peak as a function of the dopant concentration in the film.

undoped ZnO < IZO < AZO < GZO, showing that, in all cases, the doping results in an increase of the free carrier density. The spectra were used to extract the optical bandgap,  $E_{g'}$  of the materials via Tauc plots [28], which are shown in Fig. 8e. In these plots, we use the Tauc relation for a direct bandgap semiconductor (Eq. 1) to fit the experimental curves.

$$\alpha(h\nu) = \frac{A(h\nu - E_g)^{\frac{1}{2}}}{h\nu} \quad (1)$$

Equation 1 describes the dependence of the absorption coefficient,  $\alpha$ , on the photon energy  $h\nu$  (where  $h$  is Planck's constant and  $\nu$  the photon frequency), with  $A$  being a constant. The bandgap value is the intercept of the linear fit of the experimental curves (for energies above the bandgap) with the  $h\nu$ -axis. The onset of the interband transition is shifted due to the Burstein–Moss effect from 3.37 eV for the undoped ZnO film up to 3.5 eV for the AZO-3 sample. As can be seen in Fig. 8f, Al doping caused the biggest bandgap shift, followed by Ga and, last, In. This is in accordance with the observation of Sans et al. [29]. They report that antibonding dopant metal O states hybridize with the ZnO conduction band, leading to a reduction in the bandgap. The degree of this perturbation, and thus the reduced bandgap, was found to be smallest for Al and largest for In, matching the experimental results. The bandgap increases significantly for low concentration of dopants and varies only slightly with further addition of dopants.

The effects of dopant incorporation into the ZnO films were additionally probed by analyzing the exponential tail of the absorption coefficient below the bandgap energy, which can be described by Urbach equation (Eq. 2).

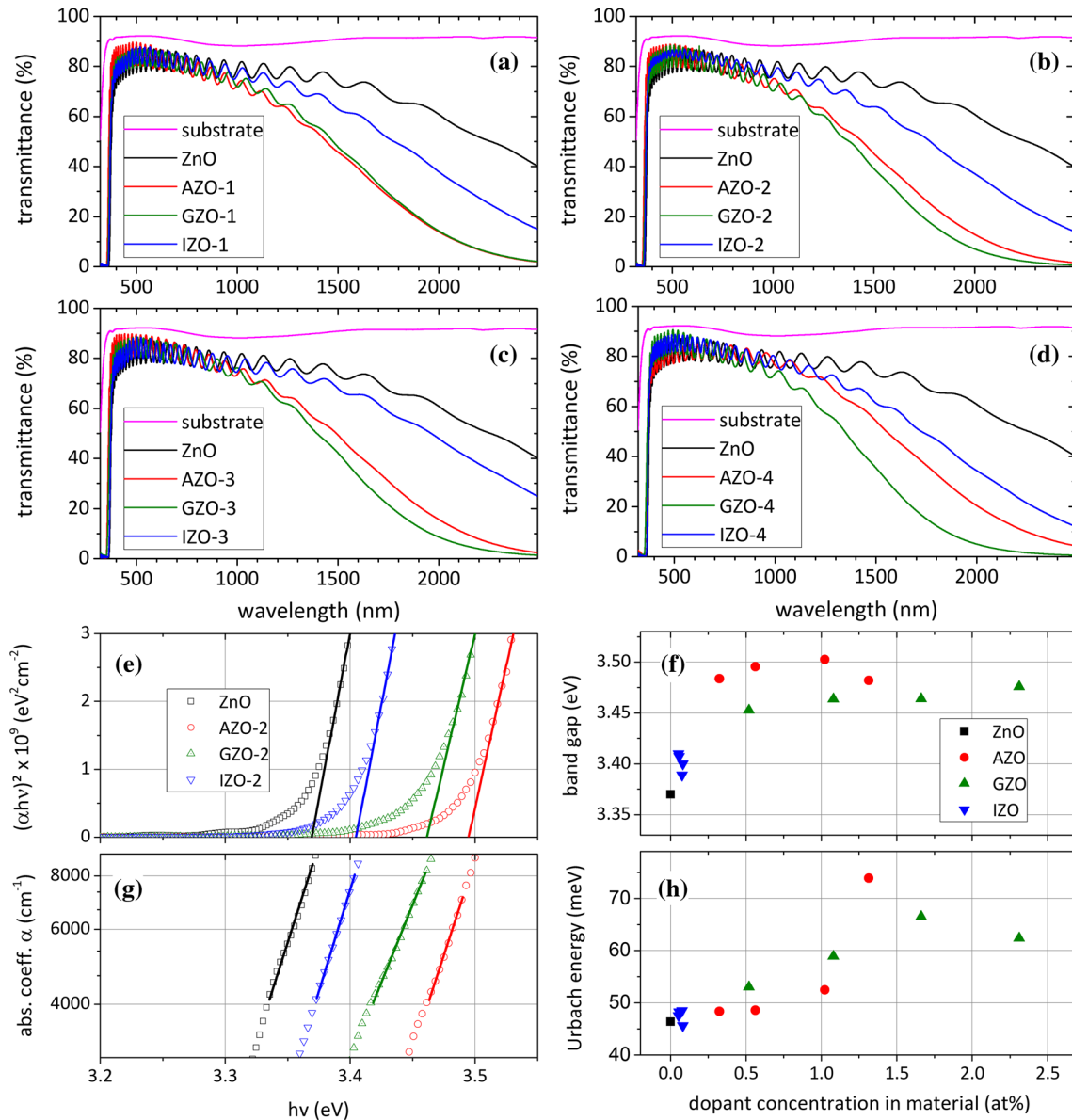


**Figure 8** a–d Transmittance spectra for the undoped and doped ZnO films. e Typical Tauc plots for a set of undoped and doped films. f Extracted bandgap values for all investigated films.

$$\alpha(h\nu, T) = \alpha_0 \exp\left(\frac{h\nu - E_0}{E_u(T, X)}\right) \quad (2)$$

The width of the exponential tail is represented by the empirical parameter  $E_u$ , termed as Urbach energy, with  $\alpha_0$  and  $E_0$  being constants.  $E_u$  depends on the disorder induced by the temperature,  $T$ , and by structural defects or impurities,  $X$ . The temperature and defect contributions can be viewed as independent according to Cody et al. [30]. As the spectra have been recorded at constant temperature, differences in  $E_u$  arise from the structural

g Semilogarithmic plots of the absorption coefficient versus photon energy, used to extract the Urbach energies. h Extracted Urbach energies for all investigated films.

disorder in the ZnO host lattice, which is induced primarily by the incorporation of dopant atoms.  $E_u$  also depends on the actual free carrier density in the films, as electron interactions both among themselves and with the positive impurity ions cause a deformation of the parabolic bands of the unperturbed semiconductor, which in turn results in band tailing [31]. Experimental curves such as the ones shown in Fig. 8g were fitted to Eq. 2, and the  $E_u$  was finally calculated as the inverse slope of the linear segment, for energies below the bandgap



[32]. Figure 8h summarizes the obtained Urbach energies for all samples. The undoped ZnO sample shows the lowest value of 46 meV, which increases upon dopant introduction to a level of 74 meV for the AZO-4 sample. The general dependence of the Urbach energy on the type and concentration of the dopant agrees with the dependence of the (002) peak shift was observed in the XRD measurements (Fig. 4b). This suggests that at least one of the responsible mechanisms behind both observations is the lattice distortion caused by the dopant introduction in the films. Nevertheless, contrary to the XRD peak shift,  $E_u$  is also influenced by the free carrier density and so, the observed differences between the Al-, Ga- and In-doped samples should also reflect this factor. The Ga-doped films exhibit the highest free carrier density as we will see later, which leads, in combination with strong lattice distortion, to more pronounced band tailing than Al-doped films. The situation is reversed only for the AZO-4 sample, as it presents a significantly perturbed growth (Fig. 4b).

The optical carrier density,  $N_{opt}$ , and mobility,  $\mu_{opt}$ , of the films were extracted by fitting optical reflectivity spectra to the Drude theoretical model, described by Eqs. 3–9 [33].

$$R = \frac{(N - 1)^2 + K^2}{(N + 1)^2 + K^2} \quad (3)$$

$$N = \sqrt{\frac{1}{2}(\epsilon_1^2 + \epsilon_2^2)^{\frac{1}{2}} + \frac{\epsilon_1}{2}} \quad (4)$$

$$K = \sqrt{\frac{1}{2}(\epsilon_1^2 + \epsilon_2^2)^{\frac{1}{2}} - \frac{\epsilon_1}{2}} \quad (5)$$

$$\epsilon_1 = \epsilon_\infty \left( 1 - \frac{\omega_p^2 \tau^2}{1 + \omega^2 \tau^2} \right) \quad (6)$$

$$\epsilon_2 = \epsilon_\infty \frac{\omega_p^2 \tau}{\omega(1 + \omega^2 \tau^2)} \quad (7)$$

$$\mu_{opt} = \frac{\tau e}{m^*} \quad (8)$$

$$N_{opt} = \frac{\left( \omega_p^2 + \frac{1}{\tau^2} \right) \epsilon_\infty \epsilon_0 m^*}{e^2} \quad (9)$$

In these equations,  $R$  is the reflectivity,  $N$  and  $K$  the real and imaginary parts of the complex refractive index,  $\epsilon_1$  and  $\epsilon_2$  the real and imaginary parts of the complex permittivity,  $\epsilon_\infty = 3.75$  the high-frequency permittivity of ZnO,  $e$  the elementary charge,  $\omega$  the

angular frequency,  $\omega_p$  the plasma frequency and  $m^* = 0.28m_e$  [34] the effective electron mass of ZnO (with  $m_e$  the free electron mass).  $\mu_{opt}$  is extracted from the fitting parameter  $\tau$ , which represents the mean free time between electron collision events, whereas  $N_{opt}$  is derived from both the plasma frequency and  $\tau$ .

Typical reflectivity spectra measured for the ZnO, AZO-2, GZO-2 and IZO-2 samples are shown along with the respective fits to the Drude model in Fig. 9. The obtained  $N_{opt}$  and  $\mu_{opt}$  values are plotted as a function of the dopant concentration in the film in Fig. 10a, b, respectively. The area of interaction in the optical characterization is considered to be in the nm range, excluding the longer-range grain boundary scattering [35].

The doping increased the carrier density, from  $3.3 \times 10^{19}$  for ZnO up to  $3.3 \times 10^{20} \text{ cm}^{-3}$  for GZO-3, and also caused a reduction in the optical mobility from 30.1 for ZnO down to 5.2  $\text{cm}^2/(\text{Vs})$  for GZO-4. The increase in carrier density is stronger in Ga-doped materials compared to Al-doped (Fig. 10a), which is in accordance with the peak shifts observed in the XRD measurements (Fig. 6d). Due to its size, Al can also be incorporated interstitially in the octahedral void in ZnO, where it does not act as donor [36]. Ga, on the other hand, is more prone to substitutional incorporation and thus introduces more efficiently charge carriers [37]. The carrier density of the IZO films is only slightly higher than for ZnO. A concomitant reduction in mobility can be observed

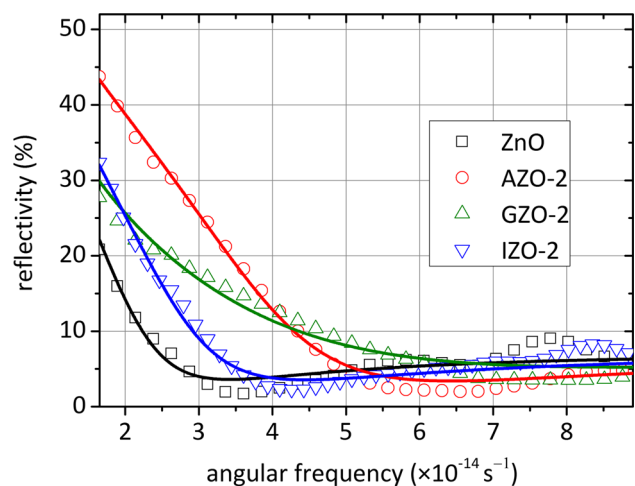


**Figure 9** Typical reflectivity spectra for a set of undoped and doped films, together with the corresponding fits to the Drude model, which was used to extract the optical carrier density and mobility values.

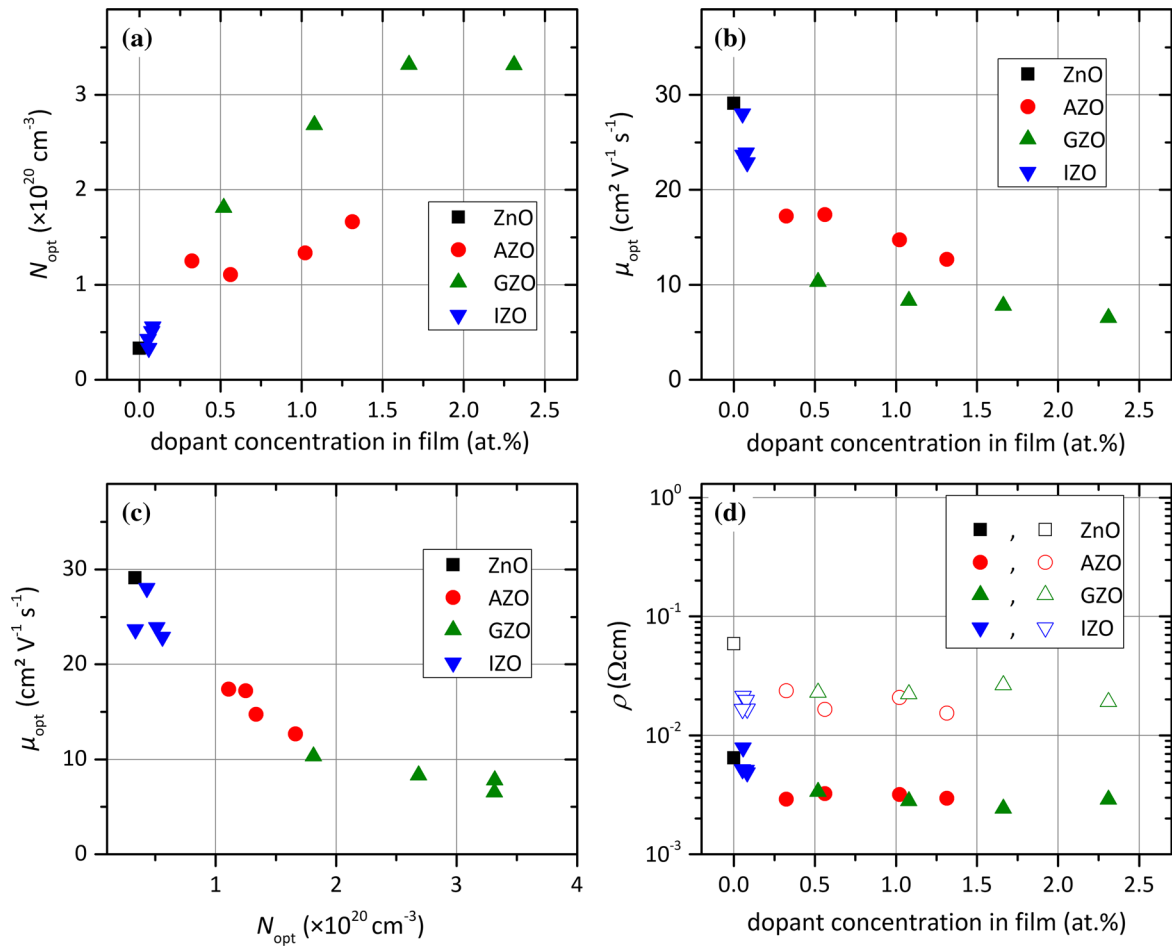


**Figure 10** Values obtained from fitting the Drude model to optical reflectivity data: **a** optical carrier density and **b** optical mobility as a function of the dopant concentration in the films. **c** Carrier

for the doped materials with increasing carrier concentration, independent of the dopant type (Fig. 10c), suggesting that ionized impurity scattering is the dominant scattering mechanism. The optical Drude model accounts only for intragrain effects. Thus, the optical DC conductivity, calculated from Eq. 10, does not take into account the grain boundary scattering, which has a major influence on the mobility of polycrystalline ZnO materials [38].

$$\sigma_0 = \frac{N_{opt}e^2\tau}{m^*} \tag{10}$$

The contribution of grain boundary scattering amounts to the difference between the optical and the electrical resistivity. The latter was obtained from standard four-point probe measurements, and the two quantities are plotted in Fig. 10d versus the dopant concentration.

density versus mobility. **d** Resistivity values of doped and undoped materials obtained by electrical four-point measurements (*open symbols*) and the optical fitting procedure (*solid symbols*).

The difference between the optical and electrical resistivity can be explained based on the model of Seto [39], where grain boundary scattering is described via a back-to-back Schottky barrier of height  $E_B$ , which is overcome by the carriers via thermionic emission. In this model, the carrier mobility is proportional to the grain size  $L$  and it exponentially depends on  $E_B$ , according to Eq. 11:

$$\mu_{GB} \propto L \exp\left(-\frac{E_B}{kT}\right) \tag{11}$$

The barrier height itself depends on the grain size, the grain boundary trap density  $Q_t$  and the carrier concentration. In polycrystalline ZnO films, the grain boundary trap density is estimated to be in the range of  $10^{12} \text{ cm}^{-2}$  for undoped ZnO [40] and reaches  $1.5\text{--}3 \times 10^{13} \text{ cm}^{-2}$  for sputtered AZO materials [38].  $E_B$  increases linearly with  $N$  to a critical value, given

by the ratio  $Q_t/L$ . After reaching this critical value, the barrier height decreases as  $1/N$  [39]. For a typical grain size of 200 nm,  $Q_t/L$  ranges with the above values from  $5 \times 10^{16} \text{ cm}^{-3}$  to  $2 \times 10^{18} \text{ cm}^{-3}$ . These numbers are at least one order of magnitude lower than the carrier concentration extracted for the present films, meaning that a  $1/N$  decrease of the grain boundary barrier is expected in all cases. The intrinsic sample shows the largest difference between optical and electrical resistivity, which is attributed to the void-rich morphology and the smaller grain size (see Figs. 2 and 3). Additionally, this material exhibits the lowest carrier concentration, which translates to the largest grain boundary barrier, limiting its mobility to a larger extent compared to the doped films. Although In shows the lowest carrier density among doped films, it yields the lowest resistivity, with the IZO-2 sample attaining a value of  $1.7 \times 10^{-2} \Omega \text{ cm}$ . This is attributed to the larger grain size observed for the IZO films, which suppresses grain boundary scattering.

For the UV stability of the sheet resistance, the carrier concentration seems to play the determinant role. Figure 11 shows the dependence of the sheet resistance for the ZnO, AZO-2, GZO-2 and IZO-2 films, as a function of UV exposure and relaxation time, in a long-duration UV-annealing experiment. The films were exposed to  $12.1 \text{ kJ cm}^{-2}$  UVA and UVB radiation for a period of 120 h, and the evolution of sheet resistance was further monitored for 242 h after the UV exposure, with the films stored in ambient conditions. Upon illumination, the resistance shows a fast decrease typical for the persistent photoconductance effect in ZnO [41]. The strongest reduction was observed for the undoped film, which remains pronounced at the end of the illumination period. The doped films were in comparison less affected and additionally showed only a minor decrease in the last hours of illumination. The same trend could be observed in the relaxation period, where again the undoped films showed the greatest change in resistance, which quickly doubled within the first 3 h and then rose further. The resistance of the doped samples was significantly more stable in the order  $\text{IZO} < \text{AZO} < \text{GZO}$ . The later showed almost no increase in resistivity.

Generally, irradiating polycrystalline ZnO with UV light leads to an increase in conductivity, which outlasts the duration of the regular photoelectric effect. This phenomenon is explained by chemisorbed

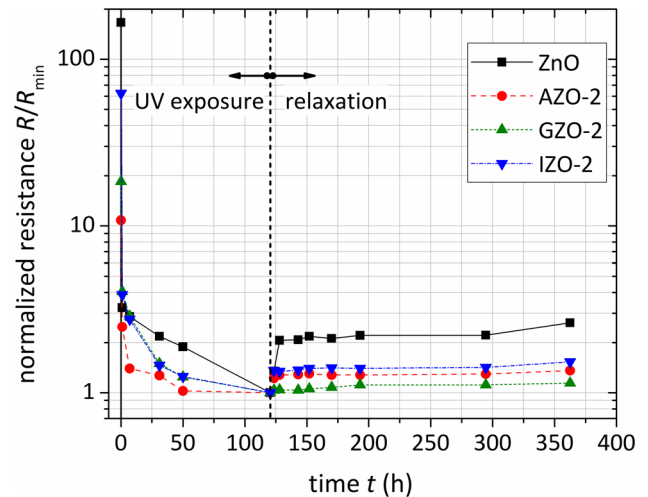


**Figure 11** Dependence of the sheet resistance values during the long-term annealing experiment, in which the samples were exposed 120 h to  $12.1 \text{ kJ/cm}^2$  UVA and UVB irradiation. The values are plotted normalized to the minimum value obtained at the end of the annealing procedure.

species such as oxygen or water, which are bonded to the ZnO surface and grain boundaries. Under UV irradiation, electron–hole pairs are formed in the material. When the holes diffuse to the surface or the grain boundaries, they can oxidize the chemisorbed species, which are present there. These species remain then either physisorbed at the position or desorb completely. As this process consumes only holes, the crystal is enriched with free electrons, increasing its conductivity. The extent of this effect depends on the number of generated free electrons, which is proportional to the grain boundary area. ZnO films, composed from nanoparticles, show for example a very pronounced effect due to their low grain size [42].

When the UV exposure is off, water and oxygen from the ambient atmosphere can reabsorb to the material, reversing the effect. The relative change of the sheet resistance is  $\Delta R/R_{\min}$ , where  $\Delta R = R_{\max} - R_{\min}$ .  $R_{\max}$  represents the resistance before the irradiation experiment and  $R_{\min}$  the minimum attained value. Table 2 shows the  $\Delta R/R_{\min}$  for each film together with the average grain size (see Fig. 3) and the carrier density (see Fig. 10).

The less compact morphology of the undoped sample might play a role in the fast resistance increase after illumination. However, for the doped materials, which were dense thin films, no clear correlation could be found between  $\Delta R/R_{\min}$  and the

**Table 2** Increase in resistance after a period of 242 h

	$\Delta R/R_{\min}$ (%)	Carrier density ( $\text{cm}^{-3}$ )	Grain size (nm)
ZnO	163	$3.3 \times 10^{19}$	230
IZO-2	53	$5.6 \times 10^{19}$	303
AZO-2	35	$1.1 \times 10^{20}$	263
GZO-2	14	$2.7 \times 10^{20}$	282

The values are relative to the minimum value obtained after the UV-annealing treatment. Additionally, the optical carrier density from Fig. 9 and the grain size (Fig. 5) are shown

grain size. On the other hand,  $\Delta R/R_{\min}$  consistently decreases with increasing carrier concentration. If we assume similar grain boundary area for all films, the amount of extra electrons produced by the UV light will be also similar. These extra carriers will lead to a more pronounced relative decrease of the sheet resistance for the films with lowest carrier concentration. This can be a possible explanation for the observed dependence of the  $\Delta R/R_{\min}$  on the carrier density. At the same time, we expect that the mobility is altered stronger by a carrier increase for materials with initially low carrier concentration due to the  $1/N$  dependence of the potential barrier for  $N > Q_t/L$ . Thus, grain boundary scattering might be a second reason for the increasing stability for higher carrier concentrations.

## Conclusion

Highly transparent doped ZnO thin films were deposited by an aqueous ammonia-based CBD approach. The influence of doping with the group-13 metals Al, Ga and In was investigated in detail, highlighting differences and similarities between the different doped films. The dopant concentration in the film showed a linear dependence on the dopant concentration in the solution for Ga and Al, with Ga showing the highest degree of incorporation. Indium exhibited very limited film incorporation due to its small solubility. The undoped films were less compact and presented a smaller grain size. The AZO film deposition rate continuously decreased with the dopant concentration in solution, whereas the effect was much less pronounced for Ga. All films grow preferentially in the (002) direction. With increasing doping, the lattice distortion rises, with the effect

being most pronounced for the GZO films, suggesting higher degree of substitutional incorporation. The optical characterization showed high transmittance in the visible range and pronounced infrared absorption for the doped samples, related to free carrier absorption. The bandgap increased for the doped films with the largest values extracted for AZO. On the other hand, the exponential tail of the absorption was more pronounced for GZO films, due to both increased lattice distortion and higher free carrier density. The optical carrier density was highest for GZO and lowest for ZnO. The carrier mobility decreased with increasing dopant concentration, indicating ionized impurity scattering within the grains. The difference between the resistivity values extracted from optical and electrical measurements showed that grain boundary scattering is especially important for the undoped film. Ga-doped films with the highest carrier concentration showed the largest stability of their resistance upon UV-light exposure.

## Acknowledgements

Open access funding provided by Graz University of Technology. This work was funded by the Austrian Climate and Energy Fund within the project *Flex!P-V.at* (Project Number: 838621) and project *print.PV* (Project Number: 845017). Michael Richter is acknowledged for technical assistance. The authors further thank Michael Nohava and Christina Führrhapper (Holzforschung Austria) for performing the ICP-OES analysis.

## Compliance with ethical standards

**Conflicts of interest** The authors declare that they have no conflict of interest.

**Electronic supplementary material:** The online version of this article (doi:10.1007/s10853-017-1104-8) contains supplementary material, which is available to authorized users.

**Open Access** This article is distributed under the terms of the Creative Commons Attribution 4.0 International License (<http://creativecommons.org/licenses/by/4.0/>), which permits unrestricted use, distribution, and reproduction in any medium, provided you give appropriate credit to the original author(s) and the source, provide a link to the

Creative Commons license, and indicate if changes were made.

**Electronic supplementary material:** The online version of this article (doi:[10.1007/s10853-017-1104-8](https://doi.org/10.1007/s10853-017-1104-8)) contains supplementary material, which is available to authorized users.

## References

- [1] Minami T (2005) Transparent conducting oxide semiconductors for transparent electrodes. *Semicond Sci Technol* 20:S35–S44. doi:[10.1088/0268-1242/20/4/004](https://doi.org/10.1088/0268-1242/20/4/004)
- [2] Lu A, Sun J, Jiang J, Wan Q (2010) Low-voltage transparent electric-double-layer ZnO-based thin-film transistors for portable transparent electronics. *Appl Phys Lett* 96:043114. doi:[10.1063/1.3294325](https://doi.org/10.1063/1.3294325)
- [3] Dong LF, Cui ZL, Zhang ZK (1997) Gas sensing properties of nano-ZnO prepared by arc plasma method. *Nanostructured Mater* 8:815–823. doi:[10.1016/S0965-9773\(98\)00005-1](https://doi.org/10.1016/S0965-9773(98)00005-1)
- [4] Wang ZL, Song J (2006) Piezoelectric nanogenerators based on zinc oxide nanowire arrays. *Science* 312:242–246. doi:[10.1126/science.1124005](https://doi.org/10.1126/science.1124005)
- [5] Spencer MS (1999) The role of zinc oxide in Cu/ZnO catalysts for methanol synthesis and the water–gas shift reaction. *Top Catal* 8:259. doi:[10.1023/A:1019181715731](https://doi.org/10.1023/A:1019181715731)
- [6] Meyers ST, Anderson JT, Hung CM et al (2008) Aqueous inorganic inks for low-temperature fabrication of ZnO TFTs. *J Am Chem Soc* 130:17603–17609. doi:[10.1021/ja808243k](https://doi.org/10.1021/ja808243k)
- [7] Mane RS, Lokhande CD (2000) Chemical deposition method for metal chalcogenide thin films. *Mater Chem Phys* 65:1–31. doi:[10.1016/S0254-0584\(00\)00217-0](https://doi.org/10.1016/S0254-0584(00)00217-0)
- [8] Richardson JJ, Lange FF (2009) Controlling low temperature aqueous synthesis of ZnO. 1. Thermodynamic analysis. *Cryst Growth Des* 9:2570–2575. doi:[10.1021/cg900082u](https://doi.org/10.1021/cg900082u)
- [9] Podlogar M, Richardson JJ, Vengust D et al (2012) Growth of transparent and conductive polycrystalline (0001)-ZnO films on glass substrates under low-temperature hydrothermal conditions. *Adv Funct Mater* 22:3136–3145. doi:[10.1002/adfm.201200214](https://doi.org/10.1002/adfm.201200214)
- [10] Hagendorfer H, Lienau K, Nishiwaki S et al (2014) Highly transparent and conductive ZnO: Al thin films from a low temperature aqueous solution approach. *Adv Mater* 26:632–636. doi:[10.1002/adma.201303186](https://doi.org/10.1002/adma.201303186)
- [11] Fuchs P, Hagendorfer H, Romanyuk YE, Tiwari AN (2015) Doping strategies for highly conductive Al-doped ZnO films grown from aqueous solution. *Phys Status Solidi A* 212:51–55. doi:[10.1002/pssa.201431145](https://doi.org/10.1002/pssa.201431145)
- [12] Kevin M, Tho WH, Ho GW (2012) Transferability of solution processed epitaxial Ga:Zno films; tailored for gas sensor and transparent conducting oxide applications. *J Mater Chem* 22:16442–16447. doi:[10.1039/C2JM32590J](https://doi.org/10.1039/C2JM32590J)
- [13] Miyake M, Fukui H, Hirato T (2012) Preparation of Al-doped ZnO films by aqueous solution process using a continuous circulation reactor. *Phys Status Solidi A* 209:945–948. doi:[10.1002/pssa.201127385](https://doi.org/10.1002/pssa.201127385)
- [14] Miyake M, Fukui H, Doi T, Hirato T (2014) Preparation of low-resistivity Ga-doped ZnO epitaxial films from aqueous solution using flow reactor. *J Electrochem Soc* 161:D725–D729
- [15] Nicholas NJ, Franks GV, Ducker WA (2012) Selective adsorption to particular crystal faces of ZnO. *Langmuir* 28:7189–7196. doi:[10.1021/la2050674](https://doi.org/10.1021/la2050674)
- [16] PHREEQC [http://wwwbrr.cr.usgs.gov/projects/GWC\\_coupled/phreeqc/](http://wwwbrr.cr.usgs.gov/projects/GWC_coupled/phreeqc/). Accessed 11 Aug 2016
- [17] Thermoddem—Thermochemical and Mineralogical Tables for Geochemical Modeling. <http://thermoddem.brgm.fr/>. Accessed 11 Aug 2016
- [18] Hancock RD, Martell AE (1989) Ligand design for selective complexation of metal ions in aqueous solution. *Chem Rev* 89:1875–1914. doi:[10.1021/cr00098a011](https://doi.org/10.1021/cr00098a011)
- [19] Chen JT, Wang J, Zhuo RF et al (2009) The effect of Al doping on the morphology and optical property of ZnO nanostructures prepared by hydrothermal process. *Appl Surf Sci* 255:3959–3964. doi:[10.1016/j.apsusc.2008.10.086](https://doi.org/10.1016/j.apsusc.2008.10.086)
- [20] Cheng JP, Zhang XB, Luo ZQ (2008) Oriented growth of ZnO nanostructures on Si and Al substrates. *Surf Coat Technol* 202:4681–4686. doi:[10.1016/j.surfcoat.2008.03.032](https://doi.org/10.1016/j.surfcoat.2008.03.032)
- [21] Kevin M, Ho GW (2013) Transmission/absorption measurements for in situ monitoring of transparent conducting Ga:ZnO films grown via aqueous methods. *J Mater Chem A* 1:14239–14245. doi:[10.1039/C3TA12461D](https://doi.org/10.1039/C3TA12461D)
- [22] Wood SA, Samson IM (2006) The aqueous geochemistry of gallium, germanium, indium and scandium. *Spec Issue Electron Met* 28:57–102. doi:[10.1016/j.oregeorev.2003.06.002](https://doi.org/10.1016/j.oregeorev.2003.06.002)
- [23] Shannon RD (1976) Revised effective ionic radii and systematic studies of interatomic distances in halides and chalcogenides. *Acta Crystallogr Sect A* 32:751–767. doi:[10.1107/S0567739476001551](https://doi.org/10.1107/S0567739476001551)
- [24] Saniz R, Xu Y, Matsubara M et al (2013) A simplified approach to the band gap correction of defect formation energies: Al, Ga, and In-doped ZnO. *J Phys Chem Solids* 74:45–50. doi:[10.1016/j.jpcs.2012.07.017](https://doi.org/10.1016/j.jpcs.2012.07.017)
- [25] Noriega R, Rivnay J, Goris L et al (2010) Probing the electrical properties of highly-doped Al:ZnO nanowire ensembles. *J Appl Phys* 107:074312. doi:[10.1063/1.3360930](https://doi.org/10.1063/1.3360930)

- [26] T-Thienprasert J, Rujirawat S, Klysubun W et al (2013) Compensation in Al-doped ZnO by Al-related acceptor complexes: synchrotron X-ray absorption spectroscopy and theory. *Phys Rev Lett* 110:055502. doi:[10.1103/PhysRevLett.110.055502](https://doi.org/10.1103/PhysRevLett.110.055502)
- [27] Brehm JU, Winterer M, Hahn H (2006) Synthesis and local structure of doped nanocrystalline zinc oxides. *J Appl Phys* 100:064311. doi:[10.1063/1.2349430](https://doi.org/10.1063/1.2349430)
- [28] Tauc J (1968) Optical properties and electronic structure of amorphous Ge and Si. *Mater Res Bull* 3:37–46. doi:[10.1016/0025-5408\(68\)90023-8](https://doi.org/10.1016/0025-5408(68)90023-8)
- [29] Sans JA, Sánchez-Royo JF, Segura A et al (2009) Chemical effects on the optical band-gap of heavily doped ZnO : M III (M = Al, Ga, In): an investigation by means of photoelectron spectroscopy, optical measurements under pressure, and band structure calculations. *Phys Rev B* 79:195105. doi:[10.1103/PhysRevB.79.195105](https://doi.org/10.1103/PhysRevB.79.195105)
- [30] Cody GD, Tiedje T, Abeles B et al (1981) Disorder and the optical-absorption edge of hydrogenated amorphous silicon. *Phys Rev Lett* 47:1480–1483. doi:[10.1103/PhysRevLett.47.1480](https://doi.org/10.1103/PhysRevLett.47.1480)
- [31] Van Mieghem P (1992) Theory of band tails in heavily doped semiconductors. *Rev Mod Phys* 64:755–793. doi:[10.1103/RevModPhys.64.755](https://doi.org/10.1103/RevModPhys.64.755)
- [32] Pejova B (2010) The Urbach–Martienssen absorption tails in the optical spectra of semiconducting variable-sized zinc selenide and cadmium selenide quantum dots in thin film form. *Mater Chem Phys* 119:367–376. doi:[10.1016/j.matchemphys.2009.08.064](https://doi.org/10.1016/j.matchemphys.2009.08.064)
- [33] Tsin F, Venerosy A, Vidal J et al (2015) Electrodeposition of ZnO window layer for an all-atmospheric fabrication process of chalcogenide solar cell. *Sci Rep* 5:8961
- [34] Ellmer K, Klein A, Rech B (2008) Transparent conductive zinc oxide. Springer, Berlin, p 103
- [35] Steinhauser J, Faÿ S, Oliveira N et al (2007) Transition between grain boundary and intragrain scattering transport mechanisms in boron-doped zinc oxide thin films. *Appl Phys Lett* 90:142107. doi:[10.1063/1.2719158](https://doi.org/10.1063/1.2719158)
- [36] Avadhut YS, Weber J, Hammarberg E et al (2012) Structural investigation of aluminium doped ZnO nanoparticles by solid-state NMR spectroscopy. *Phys Chem Chem Phys* 14:11610–11625. doi:[10.1039/C2CP41139C](https://doi.org/10.1039/C2CP41139C)
- [37] Gabás M, Landa-Cánovas A, Luis Costa-Krämer J et al (2013) Differences in n-type doping efficiency between Al- and Ga-ZnO films. *J Appl Phys* 113:163709. doi:[10.1063/1.4803063](https://doi.org/10.1063/1.4803063)
- [38] Bikowski A, Ellmer K (2014) Analytical model of electron transport in polycrystalline, degenerately doped ZnO films. *J Appl Phys* 116:143704. doi:[10.1063/1.4896839](https://doi.org/10.1063/1.4896839)
- [39] Seto JYW (1975) The electrical properties of polycrystalline silicon films. *J Appl Phys* 46:5247. doi:[10.1063/1.321593](https://doi.org/10.1063/1.321593)
- [40] Hossain FM, Nishii J, Takagi S et al (2003) Modeling and simulation of polycrystalline ZnO thin-film transistors. *J Appl Phys* 94:7768. doi:[10.1063/1.1628834](https://doi.org/10.1063/1.1628834)
- [41] Zhu Q, Xie C, Li H, Zeng D (2016) A method for modeling and deciphering the persistent photoconductance and long-term charge storage of ZnO nanorod arrays. *Nano Res* 9:2972–3002. doi:[10.1007/s12274-016-1182-y](https://doi.org/10.1007/s12274-016-1182-y)
- [42] Morfa AJ, MacDonald BI, Subbiah J, Jasieniak JJ (2014) Understanding the chemical origin of improved thin-film device performance from photodoped ZnO nanoparticles. *Sol Energy Mater Sol Cells* 124:211–216. doi:[10.1016/j.solmat.2014.02.002](https://doi.org/10.1016/j.solmat.2014.02.002)